Lab on a Chip

PAPER

View Article Online
View Journal | View Issue

Cite this: *Lab Chip*, 2022, **22**, 2766

Multifunctional microfluidic chips for the single particle inductively coupled plasma mass spectrometry analysis of inorganic nanoparticles†

Gyula Kajner, [a] Albert Kéri,[a] Ádám Bélteki,[a] Sándor Valkai,[b] András Dér,[b] Zsolt Geretovszky[c] and Gábor Galbács *[a]

Received 24th April 2022,
Accepted 27th June 2022

DOI: 10.1039/d2lc00377e

rsc.li/loc

This study aimed at exploiting the so far unexploited potential of carrying out on-line sample pretreatment steps on microfluidic chips for single particle inductively coupled plasma mass spectrometry (spICP-MS) measurements, and demonstrating their ability to practically facilitate most of the simpler tasks involved in the spICP-MS analysis of nanoparticles. For this purpose, polydimethylsiloxane microfluidic chips, capable of high-range dilution and sample injection were made by casting, using high-precision, 3D-printed molds. Optimization of their geometry and functions was done by running several hydrodynamic simulations and by gravimetric, fluorescence enhanced microscope imaging and solution-based ICP-MS experiments. On the optimized microfluidic chips, several experiments were done, demonstrating the benefits of the approach and these devices, such as the determination of nanoparticle concentration using only a few tens of microliters of sample, elimination of solute interferences by dilution, solution-based size calibration and characterisation of binary nanoparticles. Due to the unique design of the chips, they can be linked together to extend the dilution range of the system by more than a magnitude per chip. This feature was also demonstrated in applications requiring multiple-magnitude dilution rates, when two chips were sequentially coupled.

1. Introduction

Inductively coupled plasma mass spectrometry (ICP-MS) is known to be one of the most powerful atomic spectrometry techniques that is in use for the determination of trace elements or stable isotopes in various liquid samples, including solutions, nanodispersions, biological cells, *etc.*[1–3] Lab-on-a-chip microfluidic chip (MC) devices, which can be nowadays microfabricated with relative ease, provide a great opportunity for rapid and automated sample pretreatment for the analysis of very small sample volumes (nL–μL) in analytical chemistry.[4–7] In spite of the clear potential, there have only been a few attempts at combining the advantages of chip technology with the sensitivity and versatility of ICP-MS. In these efforts, microfluidic devices have been interfaced to ICP-MS with the focus on applications mainly in the fields of elemental speciation and biological sample analysis, including single cells and lyzed cell populations.[8,9]

Researchers at Hull University (England) were among the first ones to describe such interfacing. As early as in 2002, they developed microchip devices for the speciation of Cr(III), Cr(VI) and Cu(II) based on electrophoretic separation with ICP-MS detection.[10,11] Later they integrated a low flowrate crossflow nebulizer directly at the exit port of the chip and incorporated an evaporation chamber in the system in order to prevent great losses associated with spray chambers.[12] The good sensitivity, reproducibility and extremely low sample consumption of the system was demonstrated for indium solutions. The group of Yin *et al.* also fabricated and tested MCs with ICP-MS detection, first for the analysis of Pt in blood serum realizing a combined electrokinetic and hydrokinetic flow separation,[13] and then for Cd and Pb analysis in rice wine in a microflow injection setup with variable-volume sampling channels and an eight-way multi-functional valve.[14] Verboket *et al.* developed and characterized a novel microfluidic device for the generation of 40–60 μm droplets of aqueous samples in a jet stream of perfluorohexane.[15] The incorporation of a custom-built membrane desolvator was found to be necessary for perfluorohexane vapor removal, but the operation of the system was successfully demonstrated for the ICP-MS analysis of <1 μL of bovine red blood cells. Mavrakis and Pergantis[16] described standard dilution analysis with chip-

[a] *Dept. of Inorg, and Anal. Chem, Univ. of Szeged, Dóm sq. 7, H-6720 Szeged, Hungary. E-mail: galbx@chem.u-szeged.hu*
[b] *Inst. of Biophys, Biol. Res. Cent, Temesvári blvd. 62, H-6726 Szeged, Hungary*
[c] *Dept. of Opt, and Quant. Electr. Univ. of Szeged, Dóm sq. 9, H-6720 Szeged, Hungary*

† Electronic supplementary information (ESI) available. See DOI: https://doi.org/10.1039/d2lc00377e

based microfluidics on-line with ICP-MS for the example of Cd, Co, Pb, Cr determination in as little as 140 μL sample volume. Lackey *et al.* reported about an MC device that enabled ICP-MS characterization of isotachophoretically separated lanthanides.[17]

In one of the first MC-ICP-MS studies focusing on cell analysis, Wang *et al.* prepared an MC device for the on-line magnetic solid phase microextraction of cell samples. Cu, Zn, Cd, Hg, Pb and Bi elements were determined in HepG2, Jurkat T and MCF7 cell by using extraction on Fe_3O_4 at SiO_2 nanoparticles, surface-modified by (3-aminopropyl)-triethoxysilane (APTES) and packed in the microfluidic channels.[18] Zhang *et al.* built and successfully tested a monolithic microextraction system for the analysis of Hg, Pb and Bi in HepG2 cells and human urine samples. Ethylenediamine-modified poly(glycidyl methacrylate-*co*-ethylene glycol dimethacrylate) (poly(GMA-*co*-EDMA-NH_2)) capillary monolithic columns were embedded in the microchannels. The chips could process 16 samples in one hour.[19] On-line preconcentration of Pt(IV), Au(III) and Bi(III) using magnetic organic porous polymers was also successfully demonstrated in ref. 20. The same group also reported about the construction of MCs for the study of the uptake of nanoparticles (NPs) by HeLa cells,[21] the release of Fe and Pt from HepG2 cells that previously were treated with FePt NPs,[22] and the determination of Zn in single HepG2 cells,[23] and the development of an ion-imprinted monolithic capillary microextraction chip for the analysis of Gd^{3+} in human serum and urine samples.[24] In 2019, this group, one of the most proliferic groups in the field, also wrote a review on microfluidic chip-ICP-MS for trace element and their species analysis in cells.[8] More recently, Zhou *et al.* reported about the development of a passive microfluidic system that consists of alternating straight–curved–straight microchannels and a direct infusion micronebulizer for ICP-MS analysis of lined-up single-cells, thereby eliminating the use of oil or polymer carriers. Quantitative single-cell transportation and high detection efficiency of more than 70% was realized.[25]

Single particle inductively coupled plasma mass spectrometry (spICP-MS) is a novel technique for the rapid characterization of dilute dispersions of nano- and submicron particles. The concept of spICP-MS was first described by Degueldre *et al.*[26] This technique is based on the recording of the time-resolved ICP-MS signal, where the intensity (area) of the signal peaks generated by individual NPs is proportional to the number of analyte atoms in the detected NPs, which is also proportional to the size (mass or volume) of particles. In the case of compact, single-component, spherical NPs, the measured intensity is in a cubic relation with the particle diameter. As it was shown in recent years in the literature, through the evaluation of the signal histograms, the technique can provide information about the presence, size distribution, number concentration, elemental or isotopic composition of nanoparticles.[26–28] In our previous studies, we demonstrated that not only single-component or homogenous (random) alloy spherical NPs can be analyzed, and additional information, such as the structure and aspect ratio, as well as the porosity can also be obtained by the spICP-MS method.[29–31] spICP-MS analysis takes only a couple of minutes, and the required particle concentration is small (*ca.* 10^5 mL^{-1}), thus it is becoming a more and more popular technique. For most monometallic NPs, typical size detection limits range from *ca.* 10 to 40 nm.[32] Kálomista *et al.*[33] and later Bolea-Fernandez *et al.*[34] showed that the collision/reaction cell technology can also be used advantageously in spICP-MS measurements for diminishing spectral interferences without sacrificing much of the size detection limits or precision of the obtained data. Different aspects of spICP-MS were assessed in detail in a few reviews.[28,35–38]

It is easy to see that microfluidic sample introduction carries a promise for allowing the handling of lower liquid sample volumes (μL range), automated sample preparation and calibration in spICP-MS. In spite of this potential, there have been only a few attempts so far in the community to use an MC-spICP-MS coupling for nanoparticle characterization. Among the couple of studies that can be considered to be precursors to this goal includes *e.g.* the most recent works by Gundlach-Graham *et al.*[39] and Zhou *et al.*[25] who developed microdroplet dispensers, useful *e.g.* for the calibration of spICP-MS measurements or for the introduction of single cells into the ICP-MS. The MC-ICP-MS studies, alluded to above, that performed single cell analysis (*e.g.* Wang *et al.*[21,23]) also directly contribute to these efforts.

In the present study, our goal was to develop, for the first time in the literature, PDMS microfluidic chips that can facilitate most of the simpler tasks involved in spICP-MS analysis of inorganic nanoparticles, aiming at automation in the long run. Namely, the realization of on-line dilution across several orders of magnitude, calibration and injection of μL-range liquid samples were the analytical functions implemented. Precision 3D-printed plastic molds were used for the casting of the PDMS chips, and the experimental optimization of the microfluidic patterns was also supported by hydrodynamic simulations. The performance of the chips was demonstrated by analyzing inorganic nanoparticles and nanocomposites.

2. Experimental

2.1. Instruments and devices

An Agilent 7700X inductively coupled plasma mass spectrometer (ICP-MS) was used in all experiments (Table 1). The ICP-MS gases used were high purity technical gases obtained from Messer (Bad Soden, Germany): argon (99.996% purity) and helium (99.999% purity). Sample introduction was performed through our microfluidic devices in which the flow was generated by up to three Gilson Minipuls 3 peristaltic pumps (Gilson Inc., USA), which were controlled and synchronized with a TG5011A function generator (AIM-TTI, Huntington, UK) coupled with a computer by utilizing a

Table 1 ICP-MS operating parameters

Parameter	Value
R.F. forward power:	1550 W
Plasma sampling depth:	10 mm
Plasma gas flow rate:	15 L min^{-1}
Carrier gas flow rate:	1.05 L min^{-1}
Nebulizer type:	Agilent MicroMist (concentric)
Sample uptake flow rate:	600 μL min^{-1}
Integration time for NPs:	6 ms
Integration time for solutions:	500 ms
Monitored isotopes:	^{59}Co, ^{107}Ag, ^{197}Au
Collision cell mode:	No gas

program developed by our research group for this purpose. The exit flow from the chips was pumped into the standard MicroMist nebulizer plus Peltier-cooled Scott spray chamber sample introduction system of the ICP-MS instrument. The sample uptake rate was 600 μL min^{-1}. All measurements were carried out by monitoring the signal of the ^{59}Co, ^{107}Ag and ^{197}Au isotopes.

During the spICP-MS measurements, the data acquisition software was used in time resolved analysis (TRA) mode, and the integration time (dwell time) was set to 6 ms, whereas for the measurement of solution samples, the data acquisition software was switched to analog mode, with the integration time set at 500 ms. The acquisition time was set to 60 s. Three repetitive measurements were carried out for the purpose of repeatability calculation (RSD%). Before dilution and directly before aspiration into the ICP-MS, the nanoparticle dispersions were sonicated in an ultrasonic bath for 5 min (Bransonic 300, Ney, Danbury, CT, USA) in order to eliminate particle aggregation. For the inspection of the flow conditions inside the microfluidic chips, an Optika Ti600-FL type microscope (Optika, Italy) equipped with a Kiralux monochrome CMOS scientific camera (Thorlabs Inc., USA) was used.

2.2. Materials

Cobalt and silver sample solutions were prepared from 1000 mg L^{-1} CertiPUR monoelemental standard (Merck, Germany). whereas the gold solutions were made from a 10 mg L^{-1} Inorganic Ventures precious metal standard (Christiansburg, VA, USA). In spICP-MS measurements, commercially available NP standard dispersions were used. In experiments involving Au NPs, ultra-uniform polyethylene-glycol-capped 47.8 (1.8) nm (Nano-Composix, San Diego, CA, USA) and tannic acid-capped 28.8 (3.6) nm (Ted Pella, Redding, CA, USA) gold nanosphere standards were used. The Ag nanodispersion standards utilized were tannic acid-capped, spherical nanoparticles with diameters of 43.4 (3.2), 59.0 (5.0), 82.1 (5.5), 95.7 (10.2) nm, obtained from Ted Pella (Redding, CA, USA). Also, a dispersion of binary nanoparticles with 31 (3) nm Au core, and a 15 nm thick, Ag shell was used (Nano-Composix, San Diego, California, USA).

Trace-quality de-ionized water from MilliPore Elix 10 device equipped with a Synergy polishing unit (Merck, Germany) was used for the preparation of all solutions and diluted nanodispersions. Ismatec S3 E-LFL Tygon peristaltic tubing (IDEX, Germany) with 0.27 or 0.48 mm inner diameter was used for the aspiration of liquid samples. To drive the liquid samples to and from the microfluidic chips, stainless steel capillaries with 1.2 mm outer diameter were placed in the inlet and outlet ports. For the connection of peristaltic tubing, the inlet and outlet needles and the ICP-MS nebulizer, a PFA tubing with 0.3 inner diameter (Agilent Technologies, USA) and patches prepared from silicone tubing with 1.0 mm inner diameter (Deutsch & Neumann, Germany) were applied.

2.3. Fabrication of microfluidic devices

The microfluidic chip molds were fabricated utilizing a Form 3 professional 3D printer using the "High Temp" resin of Formlabs (USA). Prior to the molding process, a thin (tridecafluoro-1,1,2,2-tetrahydrooctil)trichlorosilane layer (Gelest Inc., USA) was applied to the mold to facilitate the removal of the cured poly(dimethylsiloxane) (PDMS) from it. The chips were cast using the Sylgard 184 silicone elastomer and curing agent set (Dow Corning, USA). After the curing process, the holes for the inlet and outlet ports were punched out using sharpened stainless-steel capillaries with 1.2 mm outer diameter. The sealing of the PDMS chips to the microscope slides was done with the help of a low-pressure, cold oxygen plasma cleaner (PDC-002, Harrick Plasma, USA).

2.4. Software and data evaluation

All data processing was performed within the Agilent MassHunter (Agilent Technologies, USA), Origin (OriginLab Corp., USA), and MS Office Excel (Microsoft Corp., USA) software. Hydrodynamic simulations on flow conditions were performed utilizing the COMSOL Multiphysics software package (COMSOL Inc., USA), in which the 3D models of the patterns were created utilizing the AutoCAD (Autodesk Inc., CA, USA) and Solid Edge (Siemens PLM Software, Plano, TX, USA) engineering design software.

The evaluation of spICP-MS measurement data is based on histograms (frequency-counts diagrams), produced from the data set of each measured nanodispersion in time resolved analysis mode. Histograms from correctly set up experiments on nanodispersions consist of two peaks, the one at low counts associated with events when no nanoparticle, but the continuous background (originating from the dissolved analyte content) is detected, while the one at higher counts (particle peak) represents the nanoparticle detection events and is the basis of both the qualitative and quantitative analysis of the nanodispersion, such as particle number concentration or size determination. All background peak was fitted with an asymmetrical Poisson function, while the particle peaks were fitted with a lognormal curve. The count value derived by subtracting the mode of the background peak from the mode of the particle peak directly correlates with the characteristic mass (size) of the measured

nanoparticles. To determine the correlation, particle size calibrations were made, either by using a set of different sized nanoparticle standards, or by using solution standards with different concentrations. The principle of the latter method lies in eqn (1), (where Q is the sample volume introduced into ICP-MS per unit time, t is the integration time, c is the concentration of the sample for the element in question, x is the ratio of the isotope of interest compared to all isotopes of the element, while η is the analyte transport efficiency), which states that under an integration period (assuming constant operating circumstances) the mass of analyte isotope reaching the detector (m) can be simply described as

$$m = Q \cdot t \cdot c \cdot \eta \cdot x \quad (1)$$

The number of detected events was calculated by integrating the particle peak of the histogram. All histogram operations were carried out using unit bin sizes.

3. Results and discussion

3.1. Design considerations

Since the MCs were planned to serve the purposes of basic, repetitive tasks occurring in nanodispersion characterization by spICP-MS (*e.g.* wide range dilution, injection of small sample volumes, calibration) and they were to be directly connected to the pneumatic nebulizer of the ICP-MS instrument, thus they were designed with considerations to certain requirements. First, it was a priority to keep the internal volume of the system and dead volume of connections as low as possible, for the sake of sample conservation and a high throughput. Second, the sample outflow rate was kept equivalent to the uptake of the pneumatic nebulizer. Third, the flows were decided to be generated/controlled with precision, multi-channel peristaltic pumps, in view of multiple reasons including the potential i) to handle several chips, ii) to support the sequential coupling of chips with the possibility to interlink them with pumps (as opposed to dead-end syringe pumps) iv) to integrate the chip with the built in multi-channel peristaltic pump of ICP-MS spectrometers, iii) throughoutly rinse the system if necessary (there is no volume limitation as opposed to the case with syringe pumps). Fourth, in order to produce the several order of magnitude dilution rates that often necessary when analyzing nanodispersions and are out of reach for conventional pump control and tube diameter changes, we intended to daisy-chain the chips. Fifth, trace analytical grade chemicals and materials were used during the synthesis, in order to keep contaminations to the minimum.

Chip fabrication was done *via* the application of PDMS casting in precision 3D-printed plastic molds, and bonded to glass substrates (microscope slides), facilitated by cold oxygen plasma cleaning/treatment. In addition to the oxygen plasma treatment, the microfluidic patterns were also designed in such a way so that a relatively great area was left

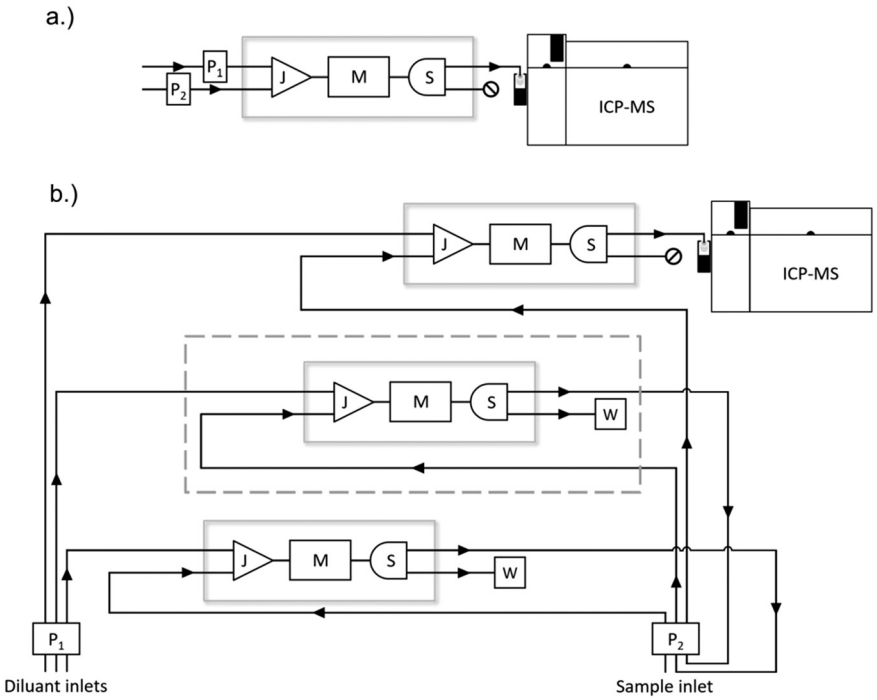

Fig. 1 Generalized schematics of the elemental units and connection of microfluidic chips. Where J, M and S are the joiner, mixer, and splitter unit respectively, P_1 and P_2 are the peristaltic pumps, supplying the diluant (1) and sample (2) flows at a fixed rate. In W, the produced waste gets collected. a) Shows the linkage used in single chip applications, while b) represents a linkage used multi-chip applications, where the segment designated by the dashed line can be built in an arbitrary number of times.

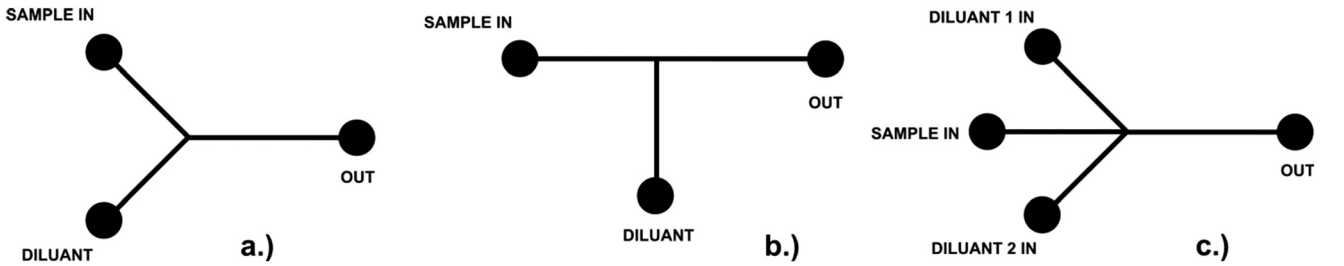

Fig. 2 A schematic representation of the three joiner designs tested. a.) "T", b.) "Y", and c.) "W" joiner.

empty on the footprint of the chips to allow for a strong bonding between the PDMS and the substrate next to channels. Rectangular channel cross sections of 350 μm height and 700 μm width (with the exception of circular port holes or special, curved segments of mixers) were chosen to be formed, which could be more precisely reproduced by 3D-printing. Comsol mechanical simulations also showed that gravitational or pressure deformation of these relatively large channels is minimal. This way, the area of the resulting channel cross sections was also similar to that of the pneumatic pump sample aspiration tube. The above considerations and approaches were all necessary to help to make the chips to withstand the pressures (2–3 bars) generated by the action of peristaltic pumps and the pneumatic nebulizer. Our chips all underwent a leak/pressure test before use and it was found that their typical burst pressure is 5.1 bar (N = 5), which is in line with the best literature values for oxygen plasma bonding,[40–42] as well as our Comsol hydrodynamic simulations.

Each chip consisted of three elementary microfluidic units: a joiner (where confluent diluant/carrier and sample input flows met), a mixer (where homogenization of the unified flow took place) and a splitter (where the homogenized flow was split into waste and output flows). Several designs for the joiner, mixer and splitter units were designed, fabricated, and tested, as it is described in detail in the following section. Initial tests about the performance of the units were always carried out on metallic standard solutions, but functional analytical chip tests were executed with nanodispersions. Fig. 1 depicts a schematic of the generalized layout and principle of connection of the chips in case of one (a) and (b) an arbitrary number of coupled chips. In the present study, single chips or two coupled chips were used.

3.2. Optimization of microfluidic functions

3.2.1. Simulation and optimization of functions

The joiner unit. For our study, the three most used joiner geometries were chosen to be tested in simulations and experiments. The T- and Y-junction designs are commonly used for relatively simple mixing steps, whereas the third, sometimes referred to as a cross-junction, but here named as the "W design" is almost exclusively used for more complicated processes, which often involve multiple phases *e.g.*, cell sorting or droplet/bubble generation.[43,44] We carried out simulations on all three designs (Fig. 2) examining the dependence of the pressure and flow conditions inside the channels on several parameters, namely the relative angle and size of the channels, as well as the total volumetric flow rate. Our simulations revealed that i) using channels of the same width is beneficial because it allows a more even pressure distribution, ii) the efficiency is constant in the volumetric flow rate range in which the chips are intended to be used, iii) using a three-channel joiner is advantageous since it facilitates the mixing by providing a higher diluant-sample surface area throughout the outlet channel.

The performance of the junction designs was assessed experimentally *via* the online dilution of a 100 ppb Co test solution, with varying dilution ratios, up to 15. The outflow was directly introduced into the nebulizer of the ICP-MS. Different dilution ratios were set by changing the relative flowrate of the sample and the diluant. Experiments were carried out in three repetitions. The repeatability of the concentration produced was below 0.4% in all cases. The relative deviation from the set (theoretical) dilution rate was 13.2%, 21.4% and 0.97% for T-, Y- and W joiners, respectively. Thus, the W-joiner performed best, thus we adapted this design in all later experiments.

The mixer unit. We designed four microfluidic patterns as mixers (Fig. 3). All these are commonly used in the literature.[45–47] Mixing in the serpentine pattern is strictly based on diffusion, while the micropillar, fishbone and Tesla valve patterns are designed to cause disturbances in the laminar flow with their protrusions, thus splitting and recombining the flow over and over. To make the mixer designs comparable, we designed them with roughly on the same footprint (*ca.* 745 mm^2). Before the production of the chips, several hydrodynamic simulations were carried out on each design in a search for potential flaws, and to assess their approximate efficiency. Some of the results are shown in Fig. 3 and Table 2, as well as in Table S1† based on which it can be stated that all four designs can successfully complete the mixing process in the tested footprint.

However, they differ in their flow resistance, internal volume and efficiency. A close observation of the concentration distribution reveals that it is the serpentine design which is the most efficient; mixing is complete after a distance of as short as a fourth of its length (area). In addition to hydrodynamic simulations, microscope-based

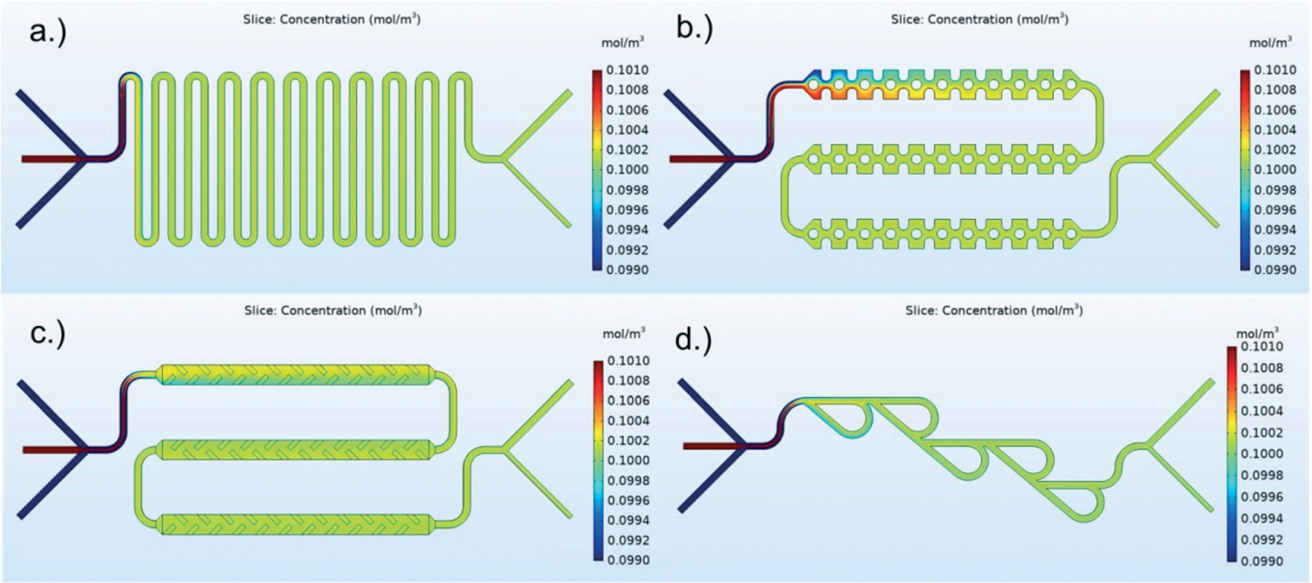

Fig. 3 Geometry of each mixer design, showing the lateral concentration profiles, plotted for the mid-height plane of the channels a.) serpentine, b.) micropillar, c.) fishbone, d.) Tesla valve, generated with the following initial parameters; sample (middle) inlet: 600 μL min^{-1}, 1 mol m^{-3}, diluant inlets: 270 μL min^{-1}, 0 mol m^{-3}.

imaging experiments using a fluorescent dye (fluorescein) were also performed. These revealed that none of the chip designs were actually able to break the laminar flow inside the channels, despite their relatively large cross section. Overall, the serpentine was found to be the best mixer, also because its simple geometry, which does not contain any constrictions or protrusions, minimizes potential problems (*e.g.*, bubbles and blockages) often occurring in soft polymer microfluidic chips. These problems were frequently observed with every other mixer design, as shown in Fig. S1.†

The splitter unit. As for the splitter, a simple design was chosen with two branches with angles of 45 degrees relative to the direction of the splitted channel. In theory, the splitting process could be simply done in a passive way, with its ratio only determined by the different flow resistance of the waste and sample outlet channels. Several papers in the literature reported about calculational methods describing fluid dynamics at the microscale along which the required chip geometries could be determined (*e.g.* Squires *et al.* and Mortensen *et al.*).[48,49] However, we decided on using forced flow (pumping) to be applied on one of the two outlet ports (sample or waste) to ensure the desired splitting ratio. The main reasons behind the decision against using a passive splitting are that otherwise i) different dilution rates would require chips with different splitter branch cross sections, ii) if linked chips are to be used, as planned, then different chips would be needed for the different positions in the daisy-chain (*e.g.* first/middle and last), iii) the system (especially coupled chips) would show a high sensitivity to random disturbances.

We also performed gravimetric experiments to find out whether the waste or sample outlet channel is more beneficial to pump. Based on five repetitions, an average of 0.67% deviation from the desired flow rate with a 0.81 RSD% was found with the pumping of the waste branch, whereas in the case of pumping the sample branch, these numbers were much improved, namely 0.01% and 0.4%. Therefore, pumping the sample outlet flow was found more beneficial. This can be explained by that the error of the pumping rate is usually proportional to the flow rate, and the sample outlet flow rate is always nine times smaller than the waste flow rate. Pumping the sample flow also has the added benefit that the increasing flow resistance of linked chips can be compensated by inserting a sample flow pump between the chips; since the sample flow rate can be fixed, this task can be handled by a multichannel pump. The finalized chip design is shown in Fig. 4.

3.2.2. Experimental testing of the injection of small sample volumes. The ability to handle samples of small volume (a few μL, nL or even fL) is one of the greatest benefits of using microfluidic devices, which synergizes well with flow injection applications.[50–52] As low volume analysis

Table 2 The internal volume of each chip design and their pressure drop according to hydrodynamic simulations

Derived data	Serpentine	Micropillar	Fishbone	Tesla valve
Pressure drop [Pa]	2319	724.1	2442	266.8
Total internal volume [μL]	101.6	70.4	43.3	31.3

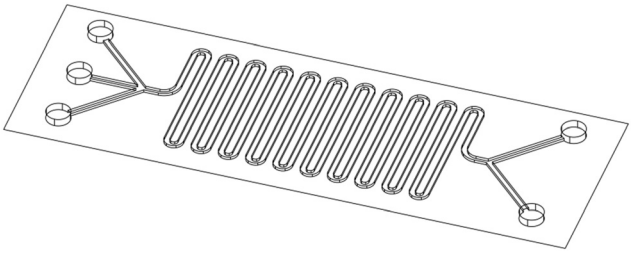

Fig. 4 The final chip design with the optimized junction, mixer and splitter units, and the capability to be coupled, used in every further experiment.

is an often-occurring task in nanoparticle characterization too, we tested our chips' ability to introduce small, well-defined volumes of samples directly to the ICP-MS to analyze. In the experiments, the diluant flows were set to 270 μL min^{-1} each, providing a sufficient, continuous flow even when no sample was injected, which is important in perspective of the ICP plasma stability. The pump responsible to the sample uptake was running continuously, delivering air or small, defined volumes of samples into the channels alternately. This causes the liquid flow to separate into distinct, low volume droplets delimited by phases of gas, which prevents longitudinal diffusion along the channel. The desired amount of sample was injected into the system in a hydrodynamic way, that is by submerging the inlet of the sample pump into the Co test solution. The time required to produce a given volume of sample was calculated based on the calibration of the peristaltic pump.

As the set of graphs in Fig. 5 show, injecting 10 to 50 μL of solution with three repetitions into the system resulted in signal profiles which correlate properly with the injected volumes (Fig. 5a), and display good repeatability (Fig. 5b). Although the FWHM of the signal profiles also showed good linearity (Fig. 5d), using integrated peak areas provided an even better fit (Fig. 5c). Based on the results, analytical results of excellent precision can be obtained by utilizing the injection function of the microfluidic device with a sample consumption as low as a few tens of microliter.

3.3. Single particle ICP-MS analysis on microfluidic chips

3.3.1. Particle concentration determination. In spICP-MS analysis, a fundamental requirement towards the measured dispersion is an optimal particle number concentration (PNC), which allows the dispersed particles to be detected individually while also keeping the frequency of the detection

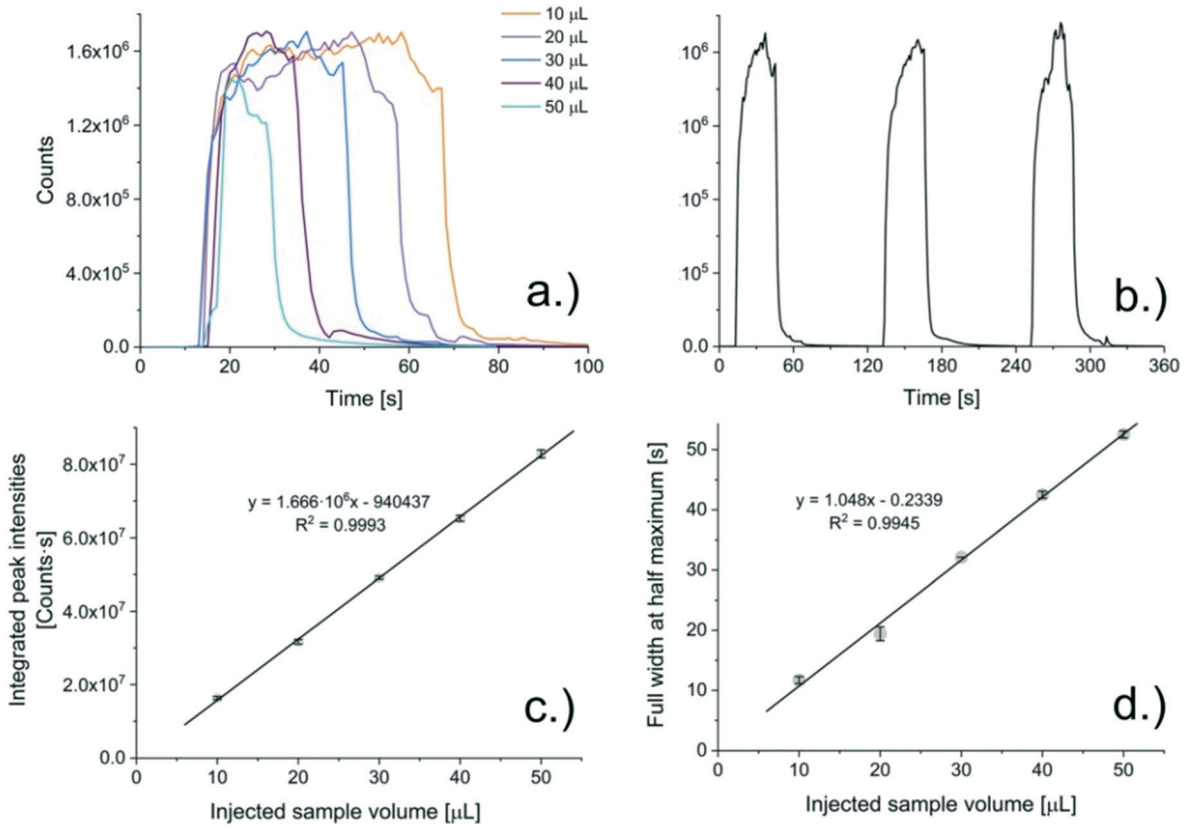

Fig. 5 Performance graphs for the injection of different volumes of a 100 ppm Co solution *via* the developed microfluidic chip. a.) Signal profiles for different sample volumes, b.) signal profiles for the repeated injection of 30 μL sample volumes, c.) integrated Co signal peak areas as a function of injected sample volume, d.) FWHM as the function of injected sample volume. All error bars are calculated based on results obtained with three repeated injections.

events relatively high for a decently low acquisition time. In case of synthetic nanodispersions, setting the required PNC *via* dilution is usually no problem, however, the concentration of real-life samples is typically not known, and its adjustment requires a lengthy manual procedure. This procedure can also be used to determine the PNC of a dispersion after establishing the correlation factor between the number of particle detection events and real PNC using a standard nanodispersion. The task can be performed in a more time-efficient and potentially a (semi)automatic way on microfluidic chips.

In order to demonstrate the performance of the chip for the dilution of nanodispersions, we measured a standard dispersion of 47.8 nm diameter Au NPs in the undiluted form as well as using on-line dilution rates of up to 10, in three repetitions. As Fig. 6a reveals, an excellent linearity between the number of detection events and the nominal PNC was found, indicating a good accuracy of the on-line dilution process.

The possibility of PNC determination was demonstrated for low volume dispersion samples too. A standard 47.8 nm Au nanodispersion of 5×10^5 mL^{-1} concentration was injected onto the chip in 10 to 50 μL discrete volumes. As results in Fig. 6b show, a good linear correlation was observed, which indicates that the proportionality between the detection events and particle concentration also holds if different sample volumes are used. The scatter of the measurement points is slightly larger than in Fig. 6a, but it is still reasonable. Note that each different point on the diagrams represents a different number of nanoparticles introduced into the instrument, except, in the case of Fig. 6a this amount was produced with fixed volumes and changing concentration, while in Fig. 6b the volume varied and the concentration was kept constant which makes the two *x*-axis comparable.

3.3.2. Elimination of solute interference. A unique property of the spICP-MS technique is that under optimal conditions, it can differentiate between the signals produced by nanoparticles and the dissolved analyte content. The particulate and dissolved forms of the analyte normally generate two distinct peaks in the signal histogram (assuming monodisperse particles), at low and medium intensities, respectively. However, in samples with a too high ionic background, the two peaks may coalesce, which renders the nanodispersion characterization not feasible. If this interference is suspected, a remedy to the situation is the dilution of the sample, which shifts the background peak towards lower counts, while leaving the particle peak in its original position since the particle size is not affected by the dilution. By utilizing the on-line diluting function of the chips, finding the right dilution rate is significantly less time-, and sample-consuming process and can potentially be automated. This possibility was demonstrated in an experiment in which a standard dispersion of 43.4 nm diameter Ag NPs with a PNC of 1×10^5 mL^{-1} also containing 1 ppb of dissolved silver was submitted to a series of dilutions. As shown in Fig. 7, the histograms of the undiluted and two times diluted samples only consist of one (coalesced) peak, while in the case of the five and tenfold dilution, the solute and particle peaks separate.

3.3.3. Solution-based size calibration. Beside the counting of nanoparticles, determining their size or the size distribution of a nanodispersion are also common analytical tasks in spICP-MS analysis. To carry out these kinds of measurements, first, a size calibration has to be made to determine the correlation between a nanoparticle of a given size (mass) and the signal induced by it. This can be executed either by measuring standard nanodispersions with different, known particle sizes or by introducing solutions (eqn (1)). The latter method is widely used due to the limited availability and/or the high price of certain standard nanoparticles. We also demonstrated that this relevant calibration method can be further simplified by utilizing the on-line dilution function of the chips. Instead of a set of

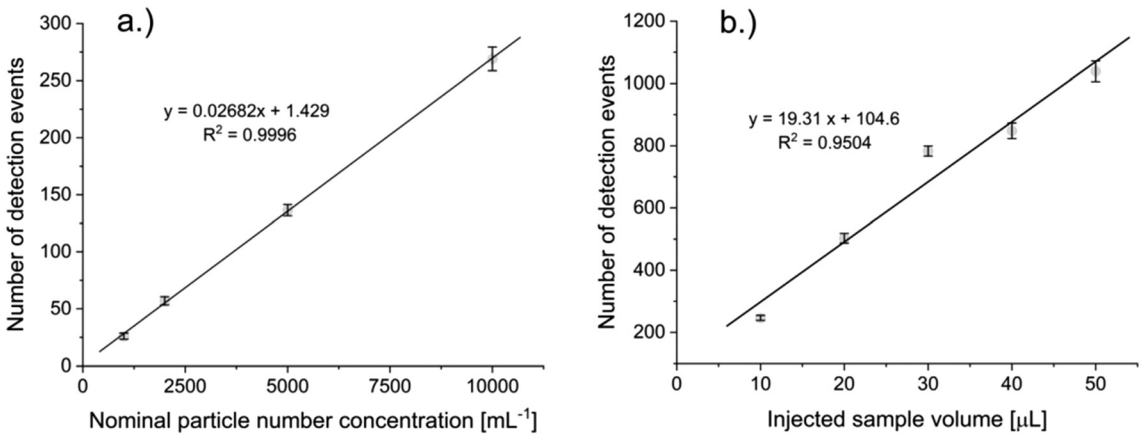

Fig. 6 a.) Correlation between the number of detection events and the nominal PNC of nanodispersions, when using a single chip for dilution. b.) Correlation between the number of detection events and the volume of the injected, 5×10^5 mL^{-1}, 48.7 nm standard Au nanodispersion into the instrument using a single chip. Error bars are calculated based on three repetitions.

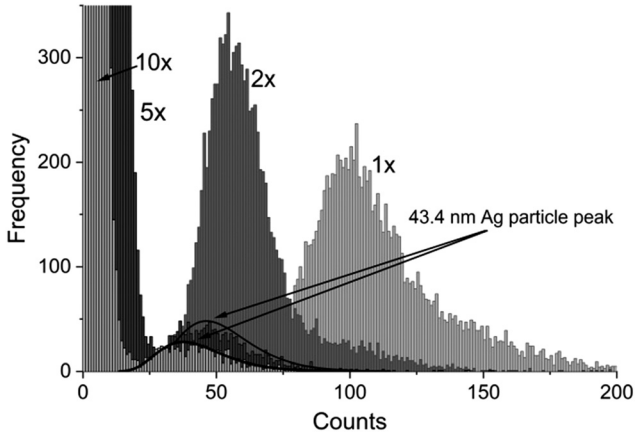

Fig. 7 Histograms of a 43.4 nm Ag nanodispersion with 1×10^5 mL^{-1} PNC and 1 ppb dissolved Ag content, measured undiluted and at 2, 5, 10-fold on-line dilution rates.

solutions with different concentration, the whole calibration procedure was done with a single 2 ppb Ag solution using dilution rates of 2, 5, 7.5, 10. The size calibration was also performed using a series of standard Ag NPs (of 43.4, 59.0, 82.1 and 95.7 nm diameter). As Fig. 8 shows, the two methods resulted in calibration curves with very similar parameters. By utilizing this method, size calibration for nanoparticles of any material can be done accurately with the use of only one standard solution.

3.3.4. Characterization of binary core–shell nanoparticles. In this next experiment, the characterization of a nanodispersion with 61 nm diameter nanoparticles which consists of a 31 nm Au core and a silver shell was done. During the execution of this analytical task, the chips were also utilized for multiple purposes supporting the analysis, including the assessment of the transport efficiency, the size calibration of both elements and producing the optimal PNC for the analysis. The particle number concentration based on

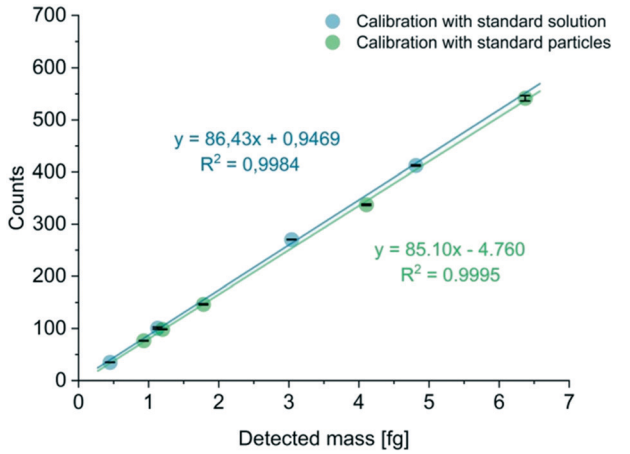

Fig. 8 Size calibrations for nanoparticle characterization, done by using a standard 2 ppb Ag solution while utilizing the chips' on-line diluting function, and using a set of standard Ag nanoparticles with diameters of 43.4, 59.0, 82.1, 95.7 nm.

Table 3 Comparison of the certified and measured core radius and shell thickness values of the standard Au–Ag core–shell nanoparticles

	(Au) core radius [nm]		(Ag) shell thickness [nm]	
	Value	Standard deviation	Value	Standard deviation
Measured	13.94	0.09	15.10	0.16
Certified	15.00	1.50	15.00	1.56

detecting both elements, as well as the average mass of Ag and Au in the particles were determined from which the core radius and the shell thickness was calculated, assuming zero porosity.[31,53,54] As shown in Table 3 the values determined by the analysis showed relatively small deviation from the value given by the certification of the standard. The two PNC values derived from counting Au and Ag detection events were determined separately and their value was found to be equal within the margin of error. This is a good indication of that these elements occur jointly in particles; a more direct proof can be obtained by using a high time resolution ICP-MS for the measurement, as our research group has shown.[55,56]

3.3.5. Measurements on two coupled chips. The on-line dilution of a high concentration Au nanodispersion was also tested on two, sequentially coupled chips in wide range (dilution rates: 2, 4, 7, 60 and 180). As Fig. 9 shows, the undiluted sample, which has the highest PNC, falls significantly behind the detection events suggested by the line function. This indicates the occurrence of co-detection events which is a result of suboptimal level of particle concentration. The dilution range of up to 200-fold provided by two sequentially coupled chips, or up to 3500-fold in the case of three, provides sufficiently large range for most tasks involved in nanoparticle characterization by spICP-MS. However, increasing the number of daisy-chained chips also results in an increased dead volume which leads to a lower sample processing rate and a higher sample consumption, thus there is a reasonable limit after which introducing

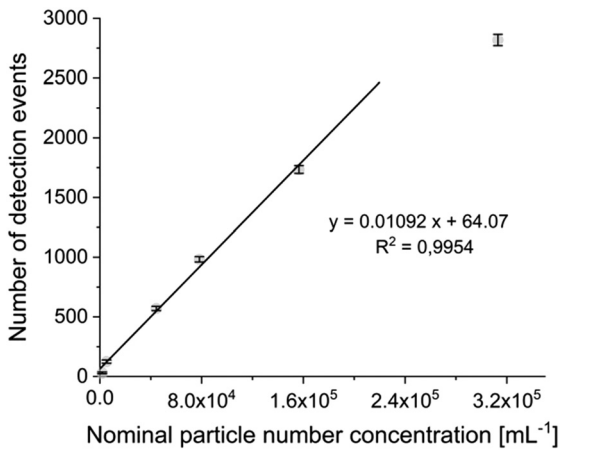

Fig. 9 The correlation between the number of detection events and the nominal PNC of nanodispersions, when using two sequentially coupled chips. Error bars are calculated based on three repetitions.

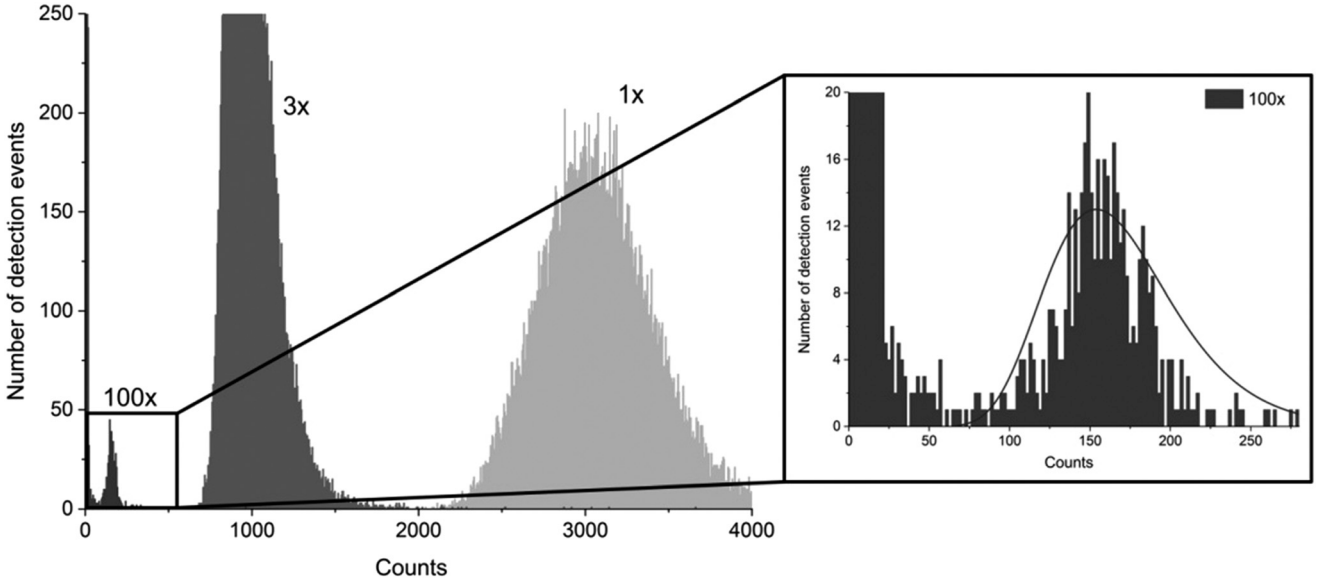

Fig. 10 Histograms of a 47.8 nm Au nanodispersion with 9.4×10^5 mL^{-1} PNC and 12 ppb dissolved Au content, measured up to 100-fold on-line dilution rate on two coupled chips. The strong dilution separates the particle peak from the background peak, thereby allowing the analysis of the nanoparticles.

additional chips into the system become detrimental to the overall performance.

The experiment described in section 3.3.2. was also done for a situation in which an even higher concentration of solute analyte is interfering with the NP characterization (47.8 nm Au NPs with a PNC of 9.4×10^5 mL^{-1}, containing 12 ppb of dissolved gold). The dispersion was on-line diluted on two, sequentially coupled chips in the range of 1 to 170-fold dilution range to optimize the measurement conditions. Using 100-fold dilution rate, the two peaks were sufficiently separated. Although the dilution rate required for the separation significantly decreased the detection frequency which resulted a quite coarse histogram, the outlines of the particle peak are still easily visible and well fittable (Fig. 10), thus PNC and particle size distribution can be determined. Data obtained using higher dilution rates are not shown, since any further dilution after peak separation only results in decreased detection frequency, which causes higher acquisition times or greater uncertainty of the determined property of the nanodispersion.

4. Conclusions

PDMS microfluidic chips were developed and fabricated for spICP-MS analysis, utilizing high precision, 3D-printed molds, and their optimization was done based on hydrodynamic simulations and experiments. By capitalizing on their ability to handle low volume samples, and to carry out injection and dilution processes over several orders of magnitude, it has been demonstrated that these chips are useful for the on-line sample pretreatment of nanodispersions, facilitating all simpler tasks involved in spICP-MS analysis. As can be seen from the presented applications, the MC-spICP-MS coupling holds great potential in nanoparticle analysis, however, given the practically unlimited possibilities of which these lab-on-a-chip devices provide due to their customizability, their true potential is yet to be explored. For this reason, our group's goal is to further develop these devices by integrating new units capable of separations.

Conflicts of interest

There are no conflicts to declare.

Acknowledgements

The authors gratefully acknowledge the financial support from various sources including the National Research, Development and Innovation Office of Hungary under No. EFOP-3.6.2-16-2017-00005, GINOP-2.3.3-15-2016-00040, TKP2021-NVA-19 and from the ÚNKP-21-2 New National Excellence Program (Gy. Kajner). The financial support received from the University of Szeged Open Access Fund under No. 5784 is also kindly acknowledged.

References

1 D. Pröfrock and A. Prange, *Appl. Spectrosc.*, 2012, **66**, 843–868.
2 F. Vanhaecke and P. Degryse, *Isotopic analysis: fundamentals and applications using ICP-MS*, John Wiley & Sons, 2012.
3 S. M. Nelms, *Inductively coupled plasma mass spectrometry handbook*, Blackwell Publishing, 2005.
4 Y. Zhu and Q. Fang, *Anal. Chim. Acta*, 2013, **787**, 24–35.
5 P. C. H. Li, *Microfluidic Lab-on-a-Chip for Chemical and Biological Analysis and Discovery*, CRC Press, 2006.

6 F. R. Walter, S. Valkai, A. Kincses, A. Petneházi, T. Czeller, Sz. Veszelka, P. Ormos, M. A. Deli and A. Dér, *Sens. Actuators, B*, 2016, **222**, 1209–1219.
7 A. Mathesz, S. Valkai, A. Újvárosy, B. Aekbote, O. Sipos, B. Stercz, B. Kocsis, D. Szabó and A. Dér, *Optofluid. Microfluid. Nanofluid.*, 2015, **2**, 15–21.
8 M. He, B. Chen, H. Wang and B. Hu, *Appl. Spectrosc. Rev.*, 2019, **54**, 250–263.
9 N. S. Ha, M. de Raad, L. Z. Han, A. Golini, C. J. Petzold and T. R. Northen, *RSC Chem. Biol.*, 2021, **2**, 1331–1351.
10 Q. J. Song, G. M. Greenway and T. McCreedy, *J. Anal. At. Spectrom.*, 2003, **18**, 1–3.
11 Q. J. Song, G. M. Greenway and T. McCreedy, *J. Anal. At. Spectrom.*, 2004, **19**, 883–887.
12 G. Pearson and G. Greenway, *J. Anal. At. Spectrom.*, 2007, **22**, 657–662.
13 H. Cheng, Z. Xu, J. Liu, X. Wang and X. Yin, *J. Anal. At. Spectrom.*, 2012, **27**, 346–353.
14 H. Cheng, J. Liu, Z. Xu and X. Yin, *Spectrochim. Acta, Part B*, 2012, **73**, 55–61.
15 P. E. Verboket, O. Borovinskaya, N. Meyer, D. Günther and P. S. Dittrich, *Anal. Chem.*, 2014, **86**, 6012–6018.
16 E. Mavrakis and S. A. Pergantis, *Anal. Chim. Acta*, 2021, **1179**, 338830.
17 H. Lackey, D. Bottenus, M. Liezers, S. Shen, S. Branch, J. Katalenich and A. Lines, *Anal. Chim. Acta*, 2020, **1137**, 11–18.
18 H. Wang, Z. Wu, B. Chen, M. He and B. Hu, *Analyst*, 2015, **140**, 5619–5626.
19 J. Zhang, B. Chen, H. Wang, M. He and B. Hu, *Anal. Chem.*, 2017, **89**, 6878–6885.
20 Z. Chen, B. Chen, M. He, H. Wang and B. Hu, *Microchim. Acta*, 2019, **186**, 107.
21 H. Wang, B. Chen, M. He, X. Li, P. Chen and B. Hu, *Talanta*, 2019, **200**, 398–407.
22 Z. Chen, B. Chen, M. He and B. Hu, *Anal. Chem.*, 2020, **92**, 12208–12215.
23 H. Wang, B. Chen, M. He and B. Hu, *Anal. Chem.*, 2017, **89**, 4931–4938.
24 X. Ou, M. He, B. Chen, H. Wang and B. Hu, *Analyst*, 2019, **144**, 2736–2745.
25 Y. Zhou, Z. Chen, J. Zeng, J. Zhang, D. Yu, B. Zhang, X. Yan, L. Yang and Q. Wang, *Anal. Chem.*, 2020, **92**, 5286–5293.
26 C. Degueldre and P. Y. Favarger, *Colloids Surf., A*, 2003, **217**, 137–142.
27 G. Galbács, A. Kéri, A. Kohut, M. Veres and Zs. Geretovszky, *J. Anal. At. Spectrom.*, 2021, **36**, 1826–1872.
28 M. D. Montano, J. W. Olesik, A. G. Barber, K. Challis and J. F. Ranville, *Anal. Bioanal. Chem.*, 2016, **408**, 5053–5074.
29 A. Kéri, A. Sápi, D. Ungor, D. Sebők, E. Csapó, Z. Kónya and G. Galbács, *J. Anal. At. Spectrom.*, 2020, **35**, 1139–1147.
30 I. Kálomista, A. Kéri, D. Ungor, E. Csapó, I. Dékány, T. Prohaska and G. Galbács, *J. Anal. At. Spectrom.*, 2017, **32**, 2455–2462.
31 A. Kéri, I. Kálomista, D. Ungor, Á. Bélteki, E. Csapó, I. Dékány, T. Prohaska and G. Galbács, *Talanta*, 2018, **179**, 193–199.
32 S. Lee, X. Bi, R. B. Reed, J. F. Ranville, P. Herckes and P. Westerhoff, *Environ. Sci. Technol.*, 2014, **48**, 10291–10300.
33 I. Kálomista, A. Kéri and G. Galbács, *J. Anal. At. Spectrom.*, 2016, **31**, 1112–1122.
34 E. Bolea-Fernandez, D. Leite, A. Rua-Ibarz, T. Liu, G. Woods, M. Aramendia, M. Resano and F. Vanhaecke, *Anal. Chim. Acta*, 2019, **1077**, 95–106.
35 D. Mozhayeva and C. Engelhard, *J. Anal. At. Spectrom.*, 2020, **35**, 1740–1783.
36 F. Laborda, E. Bolea, G. Cepriá, M. T. Gómez, M. S. Jiménez, J. Pérez-Arantegui and J. R. Castillo, *Anal. Chim. Acta*, 2016, **904**, 10–32.
37 F. Laborda, E. Bolea and J. Jiménez-Lamana, *Anal. Chem.*, 2014, **86**, 2270–2278.
38 K. Flores, R. S. Turley, C. Valdes, Y. Ye, J. Cantu, J. A. Hernandez-Viezcas, J. G. Parsons and J. L. Gardea-Torresdey, *Appl. Spectrosc. Rev.*, 2019, **56**, 1–26.
39 A. Gundlach-Graham and K. Mehrabi, *J. Anal. At. Spectrom.*, 2020, **35**, 1727–1739.
40 S. Satyanarayana, R. N. Karnik and A. Majumdar, *J. Microelectromech. Syst.*, 2005, **14**, 392–399.
41 R. W. R. L. Gajasinghe, S. U. Senveli, S. Rawal, A. Williams, A. Zheng, R. H. Datar, R. J. Cote and O. Tigli, *J. Micromech. Microeng.*, 2014, **24**, 075010.
42 M. A. Eddings, M. A. Johnson and B. K. Gale, *J. Micromech. Microeng.*, 2008, **18**, 067001.
43 C. Y. Lee, C. L. Chang, Y. N. Wang and L. M. Fu, *Int. J. Mol. Sci.*, 2011, **15**, 3263–3287.
44 P. Zhu and L. Wang, *Lab Chip*, 2017, **17**, 34–75.
45 C. C. Hong, J. W. Choi and C. H. Ahn, *Lab Chip*, 2004, **4**, 109–113.
46 B. Salim, K. Arumugham, G. Madhu and M. V. Athira, *BioTechnol.: Indian J.*, 2017, **13**, 150.
47 C. H. D. Tsai and X. Y. Lin, *Micromachines*, 2019, **10**, 583.
48 T. M. Squires and S. R. Quake, *Rev. Mod. Phys.*, 2005, **77**, 977.
49 N. A. Mortensen, F. Okkels and H. Bruus, *Phys. Rev. E: Stat., Nonlinear, Soft Matter Phys.*, 2005, **71**, 057301.
50 M. Trojanowicz and K. Kołacińska, *Analyst*, 2016, **141**, 2058–2139.
51 A. M. Leach, A. R. Wheeler and R. N. Zare, *Anal. Chem.*, 2003, **75**, 967–972.
52 L. F. Cai, Y. Zhu, G. S. Du and Q. Fang, *Anal. Chem.*, 2012, **84**, 446–452.
53 A. Sápi, A. Kéri, I. Kálomista, D. G. Dobó, Á. Szamosvölgyi, K. L. Juhász, Á. Kukovecz, Z. Kónya and G. Galbács, *J. Anal. At. Spectrom.*, 2017, **32**, 996–1003.
54 A. Kéri, I. Kálomista, D. Ungor, Á. Bélteki, E. Csapó, I. Dékány, T. Prohaska and G. Galbács, *Talanta*, 2018, **179**, 193–199.
55 A. Kéri, *PhD thesis*, ICP-MS-based analytical method development for the investigation of multi-component nanoparticles, University of Szeged, Hungary, 2020.
56 I. Kálomista, *PhD thesis*, Signal formation and the optimization of parameters in single particle ICP-MS, University of Szeged, Hungary, 2018.

